Predictive Current Control with Selection Vector Table Scheme for 3L-NPC Inverter

Viet Nguyen Hoang*, Duong Pham Hong, Dai Pham Duc
Faculty of Electrical and Electronics, Thuyloi University,
175 Tay Son Street, Hanoi, Vietnam
viethn@tlu.edu.vn; 2151214174@e.tlu.edu.vn; daipd@tlu.edu.vn

***Abstract*—The predictive current control (PCC) strategy has been widely applied to three-level neutral-point-clamped (3L-NPC) inverters to regulate the load current and balance the capacitor voltage. However, evaluating all 27 switching states in each sampling period imposes a significant computational burden. At the same time, current quality is sensitive to selection of weighting factors when multiple control objectives are simultaneously considered. To overcome these limitations, this paper proposes two methods, namely predictive current control with vector selection Table I (PCCT1) and vector selection Table II (PCCT2), in which only a subset of pre-selected switching states is employed for prediction and optimisation, thereby eliminating the need for weighting factor tuning in the cost function. As a result, computational complexity is significantly reduced and system stability is enhanced. The proposed PCCT methods demonstrate superior performance compared to conventional PCC under various operating conditions, ensuring accurate current tracking and consistent capacitor voltage balancing.**

***Index Terms*—3L-NPC inverter; Pre-selection vector; Predictive current control; Computational burden; Cost function.**

I. INTRODUCTION

The three-level neutral-point-clamped (3L-NPC) inverter has been extensively used in various applications, including motor drives [1]–[3] and renewable energy systems [4]–[7]. Despite its well-known advantages, reliable operation of the 3L-NPC inverter requires addressing two fundamental control challenges: load current tracking and DC link capacitor voltage balancing. Current tracking ensures accurate load current regulation under varying operating conditions, while voltage balancing maintains equal voltage distribution across the DC link capacitors. Conventional solutions typically integrate current controllers with modulation strategies to address these challenges simultaneously [8], [9]. However, their design is often complicated and the resulting performance strongly depends on system dynamics. Moreover, modulation strategies that guarantee capacitor voltage balance remain difficult to achieve [10]–[12].

In recent years, model predictive control (MPC) has emerged as a promising solution for power converters and motor drives, due to its intuitive formulation and flexibility of implementation [13]–[16]. MPC generally involves two fundamental steps: (i) predicting system behaviour based on a discrete-time model, and (ii) optimising a cost function to select the most suitable switching state. This approach allows for the direct incorporation of multiple control objectives and constraints, while being inherently compatible with digital control platforms. Consequently, predictive current control (PCC) has been widely adopted for 3L-NPC inverters to simultaneously regulate load current and balance capacitor voltages [17]–[21]. In such schemes, the cost function typically includes both current error and capacitor voltage error, while all 27 switching states of the inverter must be evaluated. However, the large number of candidate states leads to high computational complexity, which limits the real-time applicability of PCC.

To mitigate this problem, several approaches have been explored, such as the use of virtual voltage vectors [22]–[24] or triangular zoning techniques [25] to reduce the number of candidate states. Another effective strategy is the use of vector selection tables, where appropriate voltage vectors are pre-selected before predictive evaluation. This concept has already demonstrated promising results in voltage source inverters [26] and matrix converters [27]. Another research direction [28] proposes a novel predictive control architecture for three-level NPC inverters that reduces computational complexity and mitigates common-mode voltage. This approach utilises a statistical vector selection strategy to narrow the search space and enhance control performance, validated through simulations and experimental results.

To address the limitations mentioned above, this paper proposes two predictive current control schemes with vector selection tables (PCCT1 and PCCT2) specifically designed for 3L-NPC inverters. In the proposed schemes, only a subset of pre-selected switching states is considered during the prediction process, thereby avoiding the exhaustive evaluation of all 27 states. This approach not only reduces computational complexity but also eliminates the need for weighting factor adjustment in the cost function. The vector selection tables are constructed so that the selected voltage vectors inherently fulfil either the current tracking or the capacitor voltage-balancing requirement, thus mitigating the dependence on weighting factor selection. As a result, the proposed PCCT schemes ensure accurate current tracking and consistent capacitor voltage balancing, while significantly improving computational efficiency and robustness compared to conventional PCC. The simulation results

Manuscript received 19 April, 2025; accepted 8 July, 2025.

validate the effectiveness of the proposed methods under various operating conditions.

II. THE SWITCHING STATES AND OUTPUT VOLTAGE VECTORS OF 3L-NPC INVERTER

The topology of the 3L-NPC is depicted in Fig. 1. This inverter has three-phase legs, and each phase leg has four switches, S_{1x}, S_{2x}, S_{3x}, S_{4x} with $x = \{a, b, c\}$. Switching states P, O, and N, as listed in Table I, can be used to describe the operating status of the switches in the 3L-NPC inverter.

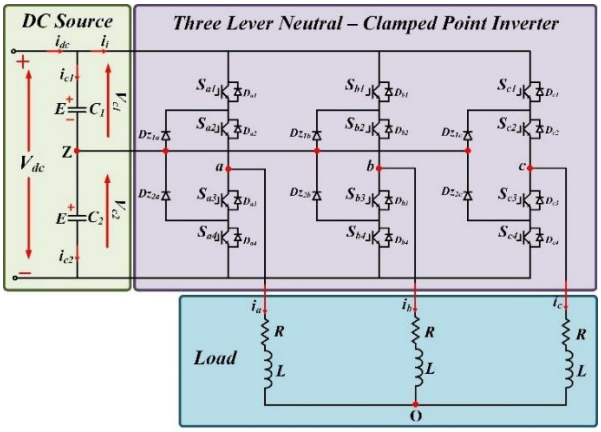

Fig. 1. The topology of the 3L-NPC inverter.

The output voltage of the 3L-NPC inverter can be calculated by switching states and the DC voltage $E = V_{DC}/2$

$$v_{xZ} = \left(S_{1x} - S_{4x}\right)E. \tag{1}$$

The output voltage vector of the inverter is defined as follows

$$\mathbf{v} = \frac{2}{3}\left(v_{aZ} + a v_{bZ} + a^2 v_{cZ}\right). \tag{2}$$

Equations (1) and (2) show that the output voltage vectors can be calculated from the switching state of the 3L-NPC inverter.

TABLE I. THE SWITCHING STATE OF THE PHASE LEG.

Switching State	S_{1x}	S_{2x}	S_{3x}	S_{4x}	v_{xZ}
P	1	1	0	0	E
O	0	1	1	0	0
N	0	0	1	1	-E

The inverter's switching state is produced by combining the switching states of its phase legs as in Table I. The 3L-NPC inverter creates 27 switching states. Each switching state produces an output voltage vector. These 27 switching states correspond to 19 voltage vectors, which are listed in Table II. The voltage vectors include six small vectors ($\boldsymbol{V_1, \ldots, V_6}$), six medium vectors ($\boldsymbol{V_7, \ldots, V_{12}}$), six large vectors ($\boldsymbol{V_{13}, \ldots, V_{18}}$), and three zero vectors ($\boldsymbol{V_{0P}, V_{0O}, V_{0N}}$). Because each small vector has two switching states, one with P and the other with N, it can be further divided into P-type small vectors ($\boldsymbol{V_{1P}, \ldots, V_{6P}}$) and N-type small vectors ($\boldsymbol{V_{1N}, \ldots, V_{6N}}$).

Table II also lists the operating states of switches S_{1x} and S_{4x} corresponding to the switching states. This information is important to represent the voltage vectors through the switching states as described in (1) and (2). The positions of the vectors are mapped onto the (αβ) coordinate system, as depicted in Fig. 2.

TABLE II. THE SWITCHING STATES AND THE ACTIVE OUTPUT VOLTAGE VECTORS.

Voltage vector	Switching State	S_{1a}	S_{4a}	S_{1b}	S_{4b}	S_{1c}	S_{4c}	$\lvert V_i \rvert$	θ_i	$V_i = v_\alpha + jv_\beta$
$\boldsymbol{V_{0P}}$	PPP	1	0	1	0	1	0	0	-	0
$\boldsymbol{V_{0O}}$	OOO	0	0	0	0	0	0	0	-	0
$\boldsymbol{V_{0N}}$	NNN	0	1	0	1	0	1	0	-	0
$\boldsymbol{V_{1P}}$	POO	1	0	0	0	0	0	$2E/3$	0	$2E/3$
$\boldsymbol{V_{1N}}$	ONN	0	0	0	1	0	1	$2E/3$	0	$2E/3$
$\boldsymbol{V_{2P}}$	PPO	1	0	1	0	0	0	$2E/3$	$\pi/3$	$E/3 + j\sqrt{3}E/3$
$\boldsymbol{V_{2N}}$	OON	0	0	0	0	0	1	$2E/3$	$\pi/3$	$E/3 + j\sqrt{3}E/3$
$\boldsymbol{V_{3P}}$	OPO	0	0	1	0	0	0	$2E/3$	$2\pi/3$	$-E/3 + j\sqrt{3}E/3$
$\boldsymbol{V_{3N}}$	NON	0	1	0	0	0	1	$2E/3$	$2\pi/3$	$-E/3 + j\sqrt{3}E/3$
$\boldsymbol{V_{4P}}$	OPP	0	0	1	0	1	0	$2E/3$	π	$-2E/3$
$\boldsymbol{V_{4N}}$	NOO	0	1	0	0	0	0	$2E/3$	π	$-2E/3$
$\boldsymbol{V_{5P}}$	OOP	0	0	0	0	1	0	$2E/3$	$-2\pi/3$	$-E/3 - j\sqrt{3}E/3$
$\boldsymbol{V_{5N}}$	NNO	0	1	0	1	0	0	$2E/3$	$-2\pi/3$	$-E/3 - j\sqrt{3}E/3$
$\boldsymbol{V_{6P}}$	POP	1	0	0	0	1	0	$2E/3$	$-\pi/3$	$E/3 - j\sqrt{3}E/3$
$\boldsymbol{V_{6N}}$	ONO	0	0	0	1	0	0	$2E/3$	$-\pi/3$	$E/3 - j\sqrt{3}E/3$
$\boldsymbol{V_7}$	PON	1	0	0	0	0	1	$2\sqrt{3}E/3$	$\pi/6$	$E + j\sqrt{3}E/3$
$\boldsymbol{V_8}$	OPN	0	0	1	0	0	1	$2\sqrt{3}E/3$	$\pi/2$	$j2\sqrt{3}E/3$
$\boldsymbol{V_9}$	NPO	0	1	1	0	0	0	$2\sqrt{3}E/3$	$5\pi/6$	$-E + j\sqrt{3}E/3$
$\boldsymbol{V_{10}}$	NOP	0	1	0	0	1	0	$2\sqrt{3}E/3$	$-5\pi/6$	$-E - j\sqrt{3}E/3$
$\boldsymbol{V_{11}}$	ONP	0	0	0	1	1	0	$2\sqrt{3}E/3$	$-\pi/2$	$-j2\sqrt{3}E/3$
$\boldsymbol{V_{12}}$	PNO	1	0	0	1	0	0	$2\sqrt{3}E/3$	$-\pi/6$	$E - j\sqrt{3}E/3$
$\boldsymbol{V_{13}}$	PNN	1	0	0	1	0	1	$4E/3$	0	$4E/3$
$\boldsymbol{V_{14}}$	PPN	1	0	1	0	0	1	$4E/3$	$\pi/3$	$2E/3 + j2\sqrt{3}E/3$
$\boldsymbol{V_{15}}$	NPN	0	1	1	0	0	1	$4E/3$	$2\pi/3$	$-2E/3 + j2\sqrt{3}E/3$
$\boldsymbol{V_{16}}$	NPP	0	1	1	0	1	0	$4E/3$	π	$-4E/3$
$\boldsymbol{V_{17}}$	NNP	0	1	0	1	1	0	$4E/3$	$-\pi/3$	$-2E/3 - j2\sqrt{3}E/3$
$\boldsymbol{V_{18}}$	PNP	1	0	0	1	1	0	$4E/3$	$-2\pi/3$	$2E/3 - j2\sqrt{3}E/3$

Based on the results in Table II and Fig. 2, the voltage vectors of the 3L-NPC inverter can be classified into four groups:

1. Zero vectors, with an amplitude of 0;
2. Small vectors, with an amplitude of $2E/3$, including six P-type vectors ($\boldsymbol{V_{1P}}$, …, $\boldsymbol{V_{6P}}$) and six N-type vectors ($\boldsymbol{V_{1N}}$, …, $\boldsymbol{V_{6N}}$);
3. Medium vectors, also with an amplitude of $2\sqrt{3}E/3$, consisting of vectors $\boldsymbol{V_7}$ to $\boldsymbol{V_{12}}$;
4. Large vectors, with an amplitude of 4E/3, consisting of vectors $\boldsymbol{V_{13}}$ to $\boldsymbol{V_{18}}$.

Zero vectors are defined as the switching states in which all three legs are identical, namely (PPP), (OOO), and (NNN). Large vectors correspond to switching state combinations composed exclusively of P- or N-type states. A total of 12 small vectors exist, characterized by switching state combinations that include the O state together with either P-type or N-type states. If the combination contains only O and N states, the corresponding small vector is classified as an N-type small vector; conversely, if the combination contains only O and P states, it is classified as a P-type small vector. Medium vectors are defined as the switching states in which all three states differ, yielding six possible combinations that correspond to six medium vectors.

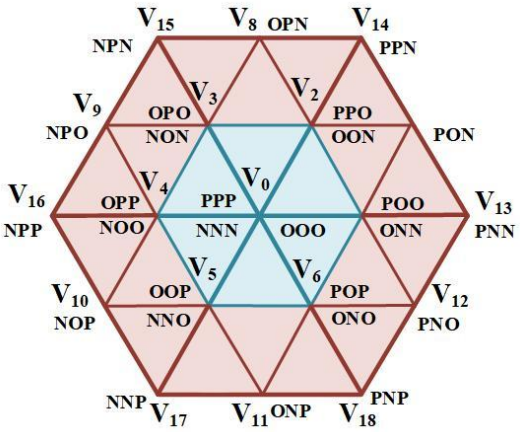

Fig. 2. Spatial distribution of vectors in the αβ plane. The PCC scheme for 3L-NPC inverter.

III. THE PCCT1 SCHEME FOR THE 3L-NPC INVERTER

The PCC scheme for the 3L-NPC inverter is illustrated in Fig. 3. Similar to conventional predictive control, the 3L-NPC inverter predictive current control involves two fundamental steps:

1. Predicting the current value;
2. Solving the cost function optimisation problem.

In this case, the predictive control algorithm must address both load current tracking and DC link capacitor voltage balancing simultaneously. To achieve these objectives, the PCC scheme uses the objective function defined in (3) [17], 18]

$$g = \left|i_\alpha^*(k+1) - i_\alpha^p(k+1)\right| + \left|i_\beta^*(k+1) - i_\beta^p(k+1)\right| + \\ +\lambda\left|\Delta V_c(k+1)\right|, \quad (3)$$

where:

– $i_\alpha^*(k+1), i_\beta^*(k+1)$ are the predictive values of the reference current on the (αβ) coordinate system, at the (k+1) sampling time;

– $i_\alpha^p(k+1)$, $i_\beta^p(k+1)$ are the predictive values of the currents on the (αβ) coordinate system, at the (k+1) sampling time;

– $\Delta V_c(k+1) = V_{c1}(k+1) - V_{c2}(k+1)$ is the predictive value of the capacitor voltage error;

– λ is the weighting factor of the cost function.

The remaining problem of this control scheme is to calculate the predicted values of the load current and the voltage capacitor error.

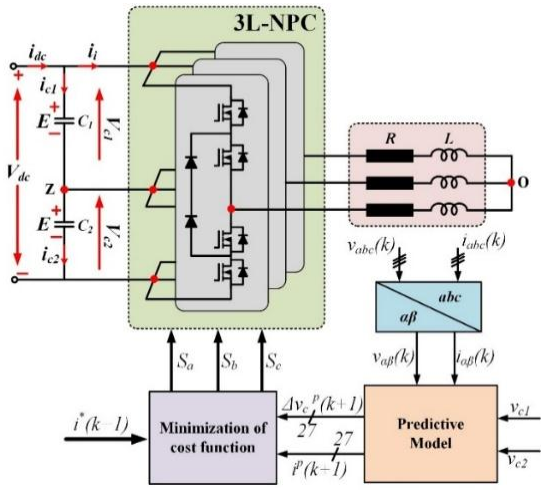

Fig. 3. The PCC scheme for the 3L-NPC inverter.

A. Predictive Model of Load Current

Consider the case of a 3L-NPC inverter with an RL load. The output current vector equation is written as in (4) [17]

$$L\frac{d\boldsymbol{i}(t)}{dt} = R\boldsymbol{i}(t) + \boldsymbol{v}(t), \quad (4)$$

where $\boldsymbol{v}(t)$ is the voltage vector of the 3L-NPC inverter, where R and L represent the load resistance and inductance, respectively, and $\boldsymbol{i}(t)$ is the load current vector

$$\boldsymbol{i}(t) = \frac{2}{3}\left(i_a + ai_b + a^2 i_c\right). \quad (5)$$

Using the Euler approximation method for (4), the discrete model of the load current is described below [17]

$$\boldsymbol{i}^p(k+1) = \frac{T}{RT+L}\left[\frac{L}{T}\boldsymbol{i}(k) + \boldsymbol{v}(k+1)\right]. \quad (6)$$

The predictive value of the load current is determined by applying (6). The predictive values of the currents in the coordinate system (αβ) are calculated as in (7)

$$i_{\alpha,\beta}^p(k+1) = \frac{T}{RT+L}\left[\frac{L}{T}i_{\alpha,\beta}(k) + v_{\alpha,\beta}(k+1)\right]. \quad (7)$$

If the sampling time T is small enough, then $i_{\alpha,\beta}^*(k+1) \approx i_{\alpha,\beta}^*(k)$.

B. Predictive Model of Capacitor Voltage Error

Capacitor currents are given by:

$$i_{c1}(t) = C\frac{dV_{c1}}{dt}, \tag{8}$$

$$i_{c2}(t) = C\frac{dV_{c2}}{dt}. \tag{9}$$

Applying the forward Euler approximation to (8), (9) yields the discrete updates:

$$V_{c1}(k+1) = V_{c1}(k) + \frac{T}{C}i_{c1}(k), \tag{10}$$

$$V_{c2}(k+1) = V_{c2}(k) + \frac{T}{C}i_{c2}(k). \tag{11}$$

Subtracting (11) from (10) gives the predictive update for the capacitor voltage error

$$\Delta V_c(k+1) = \Delta V_c(k) + \frac{T}{C}\Delta i_c(k), \tag{12}$$

where $\Delta V_c(k) = V_{c1}(k) - V_{c2}(k)$ and $\Delta i_c(k) = i_{c1}(k) - i_{c2}(k)$.

Capacitor currents are obtained from load currents and current switching state as:

$$i_{c1}(k) = i_{dc}(k) - S_{1a}i_a(k) - S_{1b}i_b(k) - S_{1c}i_c(k), \tag{13}$$

$$i_{c2}(k) = i_{dc}(k) - S_{4a}i_a(k) - S_{4b}i_b(k) - S_{4c}i_c(k). \tag{14}$$

Subtracting (14) from (13) yields

$$\Delta i_c(k) = -(S_{1a}+S_{4a})i_a(k) - (S_{1b}+S_{4b})i_b(k) - \\ -(S_{1c}+S_{4c})i_c(k). \tag{15}$$

Note that the DC link current $i_{dc}(k)$ cancels out in (15). Therefore, the predicted capacitor voltage error (12) does not depend on i_{dc}, and an additional sensor to measure i_{dc} is not required under the present modelling assumptions.

IV. THE PCCT1 SCHEME FOR THE 3L-NPC INVERTER

In this section, the PCCT1 scheme for the 3L-NPC inverter is presented, as illustrated in Fig. 4. In this method, the voltage vectors are pre-selected through the vector selection Table I. The table is constructed based on the RL load characteristics and ensures that the selected vectors inherently satisfy the current tracking requirement. Consequently, the cost function in this scheme only includes the capacitor voltage error term, as given in (16), thereby eliminating the need for weighting factor selection in the objective function

$$g_1 = \left|\Delta V_c(k+1)\right|. \tag{16}$$

The pre-selection vectors are based on current information at the load current. Suppose that the sampling time T is small and $RT \ll L$, the RT component in (7) can be ignored. Equation (7) is rewritten as follows

$$i^p_{\alpha,\beta}(k+1) - i_{\alpha,\beta}(k) = \frac{T}{L}v_{\alpha,\beta}(k+1). \tag{17}$$

The auxiliary variables d_α and d_β are defined as follows:

$$d_\alpha = i^*_\alpha(k) - i_\alpha(k), \tag{18}$$

$$d_\beta = i^*_\beta(k) - i_\beta(k). \tag{19}$$

From (17)–(19), some conclusions can be obtained as follows.

– If $i^*_\alpha(k) > i_\alpha(k)$ or $d_\alpha > 0$, then it must be guaranteed that $i^p_\alpha(k+1) > i_\alpha(k)$. From (17), the control vectors selected must have a component $v_\alpha(k+1) > 0$.

– If $i^*_\alpha(k) < i_\alpha(k)$ or $d_\alpha < 0$, then it must be guaranteed that $i^p_\alpha(k+1) < i_\alpha(k)$. From (17), the control vectors selected must have a component $v_\alpha(k+1) < 0$.

– If $i^*_\beta(k) > i_\beta(k)$or $d_\beta > 0$, then it must be guaranteed that $i^p_\beta(k+1) > i_\beta(k)$. From (17), the control vectors selected must have a component $v_\beta(k+1) > 0$.

– If $i^*_\beta(k) < i_\beta(k)$ or $d_\beta < 0$, then it must be guaranteed that $i^p_\beta(k+2) < i_\beta(k)$. From (17), the control vectors selected must have a component $v_\beta(k+1) < 0$.

From the four conclusions obtained above and observing Table II, the vector selection Table I is easily established as Table III.

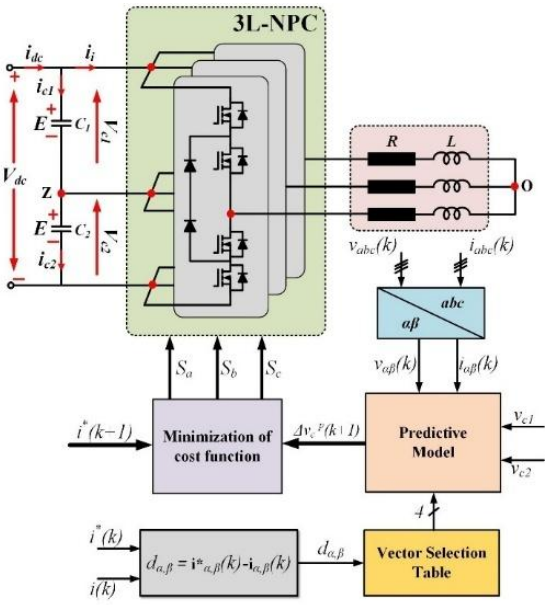

Fig. 4. The PCCT1 scheme for the 3L-NPC inverter.

TABLE III. THE VECTOR SELECTION TABLE OF THE PCCT1 SCHEME.

	$d_\beta > 0$	$d_\beta < 0$
$d_\alpha > 0$	$\boldsymbol{V_{2P}, V_{2N}, V_7, V_{14}}$	$\boldsymbol{V_{6P}, V_{6N}, V_{12}, V_{18}}$
$d_\alpha < 0$	$\boldsymbol{V_{3P}, V_{3N}, V_9, V_{15}}$	$\boldsymbol{V_{5P}, V_{5N}, V_{10}, V_{17}}$

At each control cycle, the PCCT1 scheme employs four vectors, consisting of a small P-type vector, a small N-type vector, a medium vector, and a large vector. This selection significantly reduces the computational burden of the control structure. However, the use of a limited number of vectors inherently narrows the control range of the system.

V. THE PCCT2 SCHEME FOR THE 3L-NPC INVERTER

Figure 5 illustrates the PCCT2 scheme, in which voltage vectors are selected through the vector selection Table II. This table is constructed on the basis of the analysis of the impact of voltage vectors on capacitor voltage balancing. The selected vectors inherently ensure that the capacitor voltages are maintained within a hysteresis band defined by the hysteresis controller. Consequently, the capacitor voltage-balancing requirement is excluded from the cost function, which only needs to address the current tracking objective. Therefore, the need for weighting factor selection in the cost function (20) is also eliminated

$$g_2 = \left|i_\alpha^*(k+1) - i_\alpha^p(k+1)\right| + \left|i_\beta^*(k+1) - i_\beta^p(k+1)\right|. \quad (20)$$

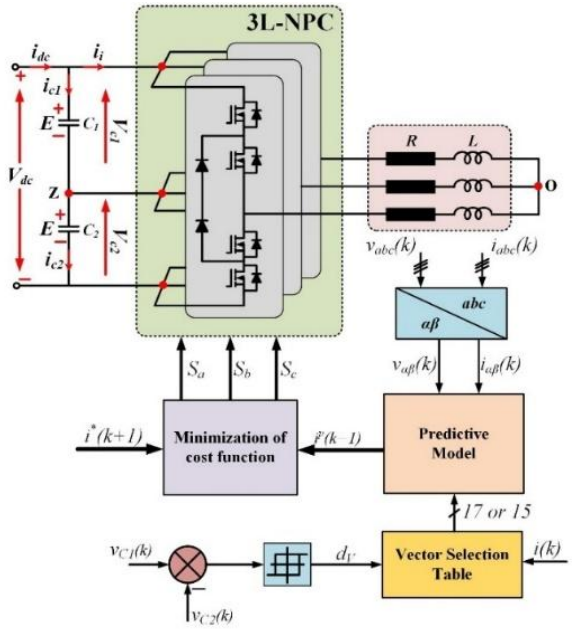

Fig. 5. The PCCT2 scheme for the 3L-NPC inverter.

Equation (12) is transformed

$$\Delta V_c(k+1) - \Delta V_c(k) = \frac{T}{C}\Delta i_c(k). \quad (21)$$

From (21), the capacitor voltage error at the next sampling instant is determined either by the sign of the capacitor current error Δi_c or, equivalently, by the switching states of the power devices together with the sign of the load current.

From Table II and (15), the switching states corresponding to the zero vectors and the large vectors result in $\Delta i_C(k) = 0$. Therefore, these two groups of vectors do not affect the capacitor voltage error at the next sampling instant.

The groups of small and medium vectors produce $\Delta i_C(k)$ with a value equal to the load current, and the specific cases are listed in Table IV.

TABLE IV. SPECIFIC CASES OF $\Delta i_c(k)$ PRODUCED BY SMALL AND MEDIUM VECTOR GROUPS.

Δi_C	Voltage Vector
i_a	$\boldsymbol{V_{1N}, V_{4P}, V_8, V_{11}}$
i_b	$\boldsymbol{V_{2N}, V_{6P}, V_7, V_{10}}$
i_c	$\boldsymbol{V_{2P}, V_{5N}, V_9, V_{12}}$
$-i_a$	$\boldsymbol{V_{1P}, V_{4N}}$
$-i_b$	$\boldsymbol{V_{3N}, V_{6P}}$
$-i_c$	$\boldsymbol{V_{2N}, V_{5P}}$

In the PCCT2 structure, a deadband controller is employed, with $\Delta V_C(k)$ as its input. The deadband is defined as $(-\epsilon, \epsilon)$, and the controller output is dv.

Based on the control law:

– If $dv = -1$, $\Delta V_C(k)$ must increase; therefore, voltage vectors are selected to ensure $\Delta V_C(k+1) > \Delta V_C(k)$;

– Conversely, if $dv = 1$, $\Delta V_C(k)$ must decrease; thus, voltage vectors are chosen to guarantee $\Delta V_C(k+1) < \Delta V_C(k)$.

Based on these observations and the information summarised in Table IV, the voltage vector selection for the PCCT2 structure is presented in Table V. In all selection cases presented in Table V, the zero vectors and large vectors are always included. Therefore, only the small and medium vectors are explicitly listed, while the zero and large vectors are implicitly understood to be consistently selected.

TABLE V. THE VOLTAGE VECTOR SELECTION FOR THE PCCT2 STRUCTURE IS PRESENTED.

	$d_V = -1$	$d_V = 1$
$i_a > 0, i_b > 0, i_c < 0$	$\boldsymbol{V_{1N}, V_{2N}, V_{3N}, V_{4P}, V_{5P}, V_{6P}, V_7, V_8, V_{10}, V_{11}}$	$\boldsymbol{V_{1P}, V_{2P}, V_{3P}, V_{4N}, V_{5N}, V_{6N}, V_9, V_{12}}$
$i_a > 0, i_b < 0, i_c < 0$	$\boldsymbol{V_{1N}, V_{2N}, V_{3P}, V_{4P}, V_{5P}, V_{6N}, V_8, V_{11}}$	$\boldsymbol{V_{1P}, V_{2P}, V_{3N}, V_{4N}, V_{5N}, V_{6P}, V_9, V_{12}, V_7, V_{10}}$
$i_a > 0, i_b < 0, i_c > 0$	$\boldsymbol{V_{1N}, V_{2P}, V_{3P}, V_{4P}, V_{5N}, V_{6N}, V_8, V_9, V_{11}, V_{12}}$	$\boldsymbol{V_{1P}, V_{2N}, V_{3N}, V_{4N}, V_{5P}, V_{6P}, V_7, V_{10}}$
$i_a < 0, i_b < 0, i_c > 0$	$\boldsymbol{V_{1P}, V_{2P}, V_{3P}, V_{4N}, V_{5N}, V_{6N}, V_9, V_{12}}$	$\boldsymbol{V_{1N}, V_{2N}, V_{3N}, V_{4P}, V_{5P}, V_{6P}, V_7, V_8, V_{10}, V_{11}}$
$i_a < 0, i_b > 0, i_c > 0$	$\boldsymbol{V_{1P}, V_{2P}, V_{3N}, V_{4N}, V_{5N}, V_{6P}, V_9, V_{12}, V_7, V_{10}}$	$\boldsymbol{V_{1N}, V_{2N}, V_{3P}, V_{4P}, V_{5P}, V_{6N}, V_8, V_{11}}$
$i_a < 0, i_b > 0, i_c < 0$	$\boldsymbol{V_{1P}, V_{2N}, V_{3N}, V_{4N}, V_{5P}, V_{6P}, V_7, V_{10}}$	$\boldsymbol{V_{1N}, V_{2P}, V_{3P}, V_{4P}, V_{5N}, V_{6N}, V_8, V_9, V_{11}, V_{12}}$

VI. RESULTS AND DISCUSSION

At this stage, a comparative analysis between the conventional predictive current control (PCC) strategy and the proposed control schemes is conducted through simulation. The DC link voltage of the inverter is set to $V_{DC} = 600$ V with a capacitance of $C = 470\ \mu F$. The load consists of a resistor and an inductor with respective values of R = 10 Ω and $L = 10$ mH. The sampling time is fixed at T = 10 µs, while the reference load current is defined at a frequency of 100 Hz. Considering the operation within the linear modulation region, the maximum load current that the three-level neutral-point-clamped (3L-NPC) inverter can deliver is approximately 25.4 A. The PCC scheme is evaluated for three distinct values of the cost-function weighting factor to investigate the trade-off between current tracking accuracy and capacitor voltage balancing. Specifically, simulations are performed with $\lambda = 0.1$, $\lambda = 1$, and $\lambda = 5$ under identical operating conditions. Comparative assessment is carried out using performance metrics such as transient tracking error, steady-state error, harmonic distortion, and the degree of capacitor voltage balance.

Based on the aforementioned system parameters, several scenarios are considered to investigate the performance of the

control schemes, as presented in the following section.

A. *Performance under Reference Variations*

In this section, the performance of the PCC, PCCT1, and PCCT2 schemes is evaluated in a representative scenario involving variations in the reference current. This case is selected to examine the dynamic tracking capability of the schemes, thereby providing insight into both transient and steady-state behaviour. Specifically, the reference current frequency is fixed at 100 Hz, with its amplitude initially set to 2 A and increased to 10 A at $t = 0.05$ s.

Figures 6(a) and 6(b) present the current responses of the α- and β-axis components, i_α and i_β, at $t = 0.05$ s following a step change in the reference amplitude. The plots compare the transient behaviour for all combinations of the three cost-function weighting factors ($\lambda = 0.1, 1, 5$) applied to the PCC, PCCT1, and PCCT2 control schemes. The results highlight differences in tracking speed, overshoot, and settling between the schemes and weighting choices.

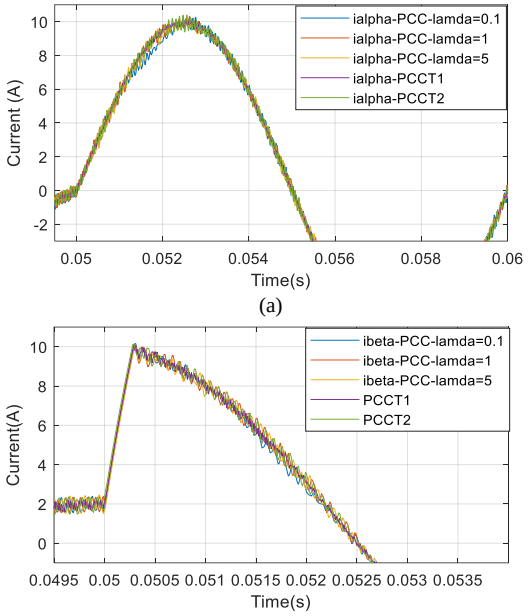

Fig. 6. Transient responses of the load currents at $t = 0.05$ s under a step change in the reference amplitude: comparison of PCC with cost-function weighting factors $\lambda = 0.1, 1, 5$, PCCT1, and PCCT2: (a) α-axis current (i_α); (b) β-axis current (i_β).

It is noted that in the Clarke transformation, the α-axis component corresponds exactly to phase-a current ($i_\alpha = i_a$). Therefore, when the amplitude of the reference current is varied, i_α immediately reflects this change. In contrast, i_β is a linear combination of i_a and i_b, which are phase-shifted by 120 °. Consequently, the adjustment of i_β requires a transient process governed by the load dynamics before reaching the new steady-state value.

The transient responses of i_α and i_β in Figs. 6(a) and 6(b) are nearly identical for the PCC, PCCT1, and PCCT2 schemes. This can be explained by the fact that all three methods utilise the complete set of voltage vectors to synthesise the desired voltage. Therefore, within the adjustable range, they are capable of producing equivalent instantaneous voltage levels during transients. As a result, no significant differences are observed in the transient behaviour when the load current reference is varied.

Figure 7 illustrates the capacitor voltages V_{C1} and V_{C2} obtained for different weighting factors λ in the PCC, PCCT1, and PCCT2 schemes. This analysis is conducted to investigate the influence of λ on the capacitor voltage-balancing performance of the control schemes considered.

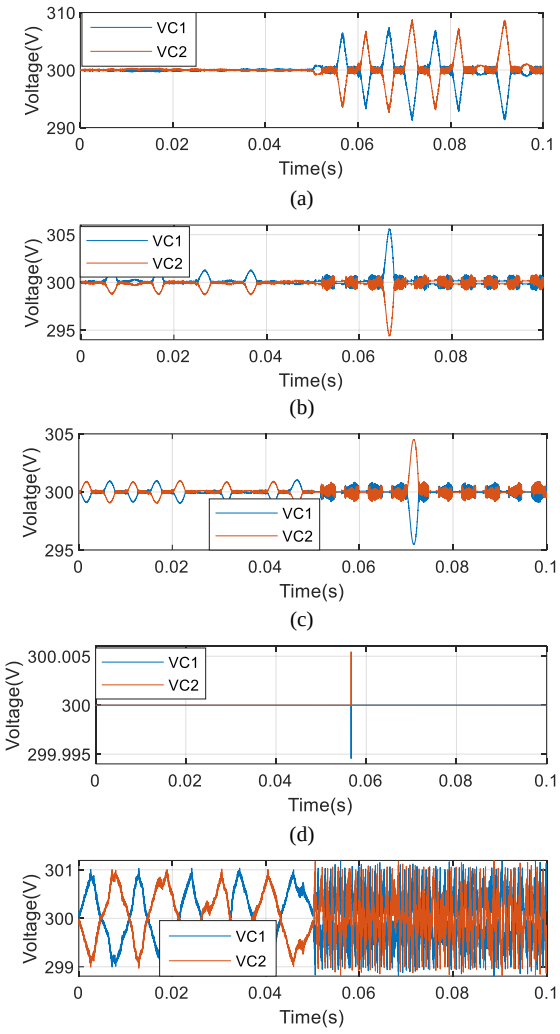

Fig. 7. Capacitor voltages V_{C1} and V_{C2}: (a) PCC with $\lambda = 0.1$; (b) PCC with $\lambda = 1$; (c) PCC with $\lambda = 5$; (d) PCCT1; (e) PCCT2.

The results in Fig. 7 indicate that the capacitor voltages remain balanced even when the reference current amplitude changes, across all three control schemes. For the PCC scheme, although the capacitor voltage balancing is maintained for different weighting factors ($\lambda = 0.1, 1, 5$), the peak-to-peak fluctuations of V_{C1} and V_{C2} vary depending on the operating point and the selected λ, as shown in Figs. 7(a)–7(c). The simulation results reveal that as the weighting factor λ increases, the peak-to-peak capacitor voltage decreases. This behaviour occurs because, with larger λ, the objective function assigns greater priority to capacitor voltage balancing.

For the PCCT1 scheme, the capacitor voltages remain nearly constant and exhibit a flat profile, as illustrated in Fig. 7(d). This behaviour can be explained by the fact that, at the operating point considered, the scheme predominantly employs zero vectors and large vectors, which do not induce variations in the capacitor voltages. However, this also implies that the inverter does not fully exploit the benefit of reduced voltage stress that can be achieved by using multiple

voltage levels.

The capacitor voltages in the PCCT2 scheme are shown in Fig. 7(e), where the values are maintained within the range of approximately 299 V–301 V. This is due to the hysteresis band used in the controller, which is set to ± 1 V. The use of the hysteresis band results in slower voltage variations, thereby reducing the fluctuation of the capacitor currents.

B. Current Tracking Performance of the Control Schemes

In this section, the tracking performance of the control schemes is evaluated in five cases, including the PCC scheme with different weighting factors ($\lambda = 0.1, 1, 5$) and the PCCT1 and PCCT2 schemes, tested at different load current operating points. The simulation results in Figs. 8–12 comprise six subplots, labelled (a) through (f). Subplots (a), (b), and (c) depict the current responses, while subplots (d), (e), and (f), respectively, present the capacitor voltages corresponding to the current cases in (a), (b), and (c).

In the simulation results of the load currents, the black dashed lines represent the reference currents i_α^* and i_β^*, while the red and blue lines denote i_α and i_β, respectively. In the simulation results of the capacitor voltages, the blue curve represents the voltage across the capacitor C_1, whereas the red curve represents the voltage across the capacitor C_2.

The simulation results in Figs. 8–10, parts (a), (b), and (c), illustrate the responses of i_α and i_β when the reference current amplitudes are set to 5 A, 10 A, and 25 A, respectively, with weighting factors $\lambda = 0.1, 1,$ and 5 in the PCC scheme. The results indicate that the tracking performance is highly dependent on both the operating point and the selected weighting factor. Although $\lambda = 0.1$ yields the best tracking capability, a transient tracking error remains at the 10 A reference amplitude, where the actual current fails to follow the reference precisely. In particular, for $\lambda = 1$ and $\lambda = 5$, the tracking quality significantly deteriorates as the current amplitude increases, especially beyond 20 A. Therefore, it can be concluded that the PCC scheme cannot fully satisfy the tracking control objective across the entire operating range.

Furthermore, the simulation results in Figs. 8–11, parts (d), (e), and (f), show the waveforms and peak-to-peak values of the DC link capacitor voltages. In the PCC scheme, the voltage imbalance of capacitor becomes more pronounced when the weighting factor λ is small. For instance, in the case of $\lambda = 0.1$ with a reference current of 10 A, the capacitor voltage deviation reaches up to 16 V. This phenomenon can be explained by the fact that a smaller weighting factor prioritises the current tracking objective in the cost function over capacitor voltage balancing. This conclusion is further supported by the cases of $\lambda = 1$ and $\lambda = 5$, where the voltage deviation of the capacitor is significantly reduced compared to $\lambda = 0.1$; however, the current tracking performance degrades under high load currents.

Figures 11 and 12 present the simulation results of the PCCT1 and PCCT2 schemes, respectively, under different load current levels. Although PCCT1 achieves excellent tracking performance, its operating range is limited to 0 A–15 A and it fails to operate properly at higher load currents. In contrast, the PCCT2 scheme maintains stable tracking across the entire operating range, including high current levels.

Figure 11 presents the simulation results of the PCCT1 scheme at operating points of 5 A, 10 A, and 15 A. The results demonstrate that the tracking performance of PCCT1 is excellent throughout the low-current range, as illustrated in Figs. 11(a) and 11(b). However, when the operating current exceeds 15 A, such as at 20 A in Fig. 11(c), the actual current begins to deviate and fails to track the reference accurately. The capacitor voltage results indicate only minor imbalances, remaining within 2 V across the considered operating range. The observed capacitor voltage characteristics, as well as the limited current regulation capability of PCCT1, can be attributed to the reduced number of voltage vectors utilised in this control scheme compared to alternative approaches.

Figure 12 presents the simulation results of the load currents and capacitor voltages under the PCCT2 scheme. The tracking control objective is effectively achieved across the entire operating range, while capacitor voltage balancing is maintained within the hysteresis thresholds of the controller. These results highlight that PCCT2 provides significantly greater stability compared to the other two schemes.

Figure 13 presents the THD indices of phase-a, phase-b, and phase-c currents, respectively, under different operating points and for five cases: PCC with weighting factors λ = 0.1, 1, 5, PCCT1, and PCCT2.

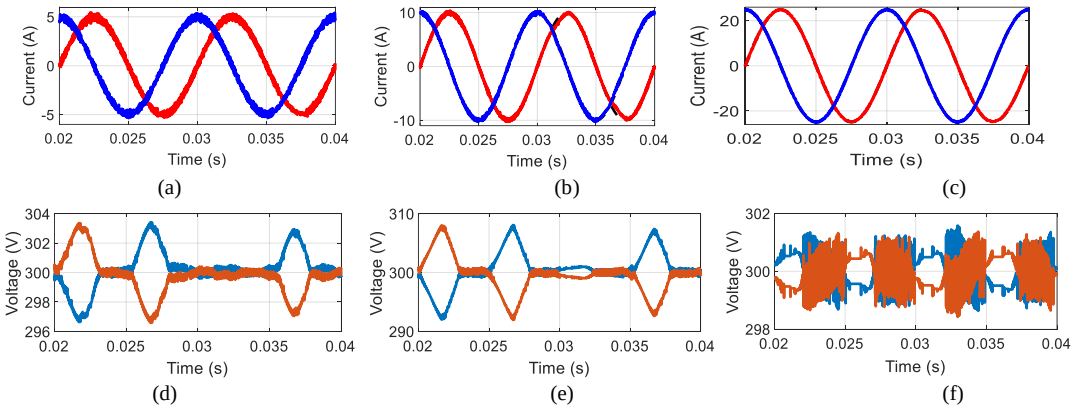

Fig. 8. Simulation results of the PCC scheme with cost function weight $\lambda = 0.1$: (a)–(c) Currents i_α, i_β for reference amplitudes of 5 A, 10 A, and 20 A; (d)–(f) Corresponding capacitor voltages: C_1 (blue) and C_2 (red).

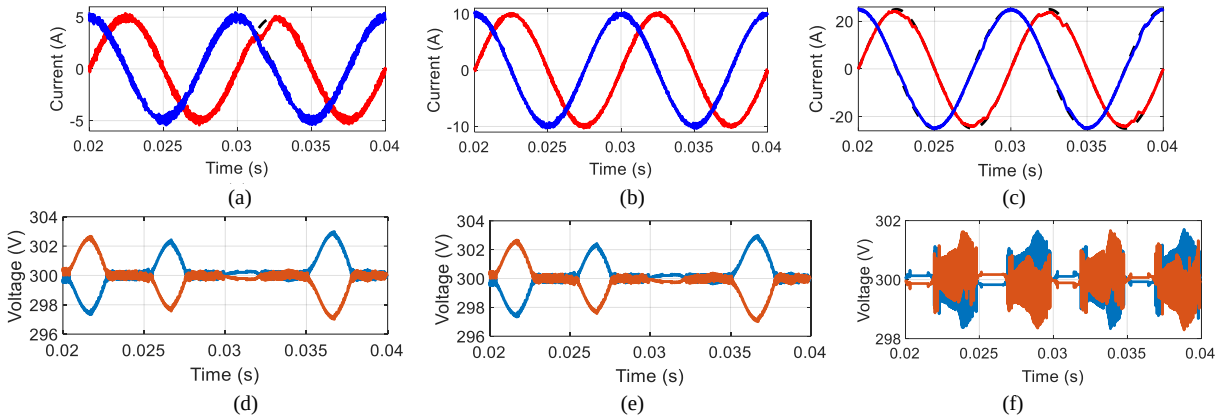

Fig. 9. Simulation results of the PCC scheme with cost function weight $\lambda = 1$: (a)–(c) Currents i_α, i_β for reference amplitudes of 5 A, 10 A, and 20 A; (d)–(f) Corresponding capacitor voltages: C_1 (blue) and C_2 (red).

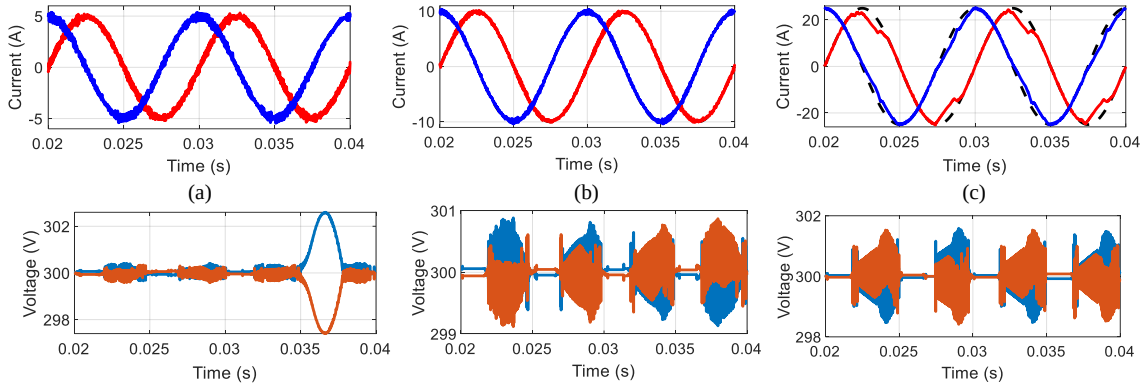

Fig. 10. Simulation results of the PCC scheme with cost function weight $\lambda = 5$: (a)–(c) Currents i_α, i_β for reference amplitudes of 5 A, 10 A, and 20 A; (d)–(f) Corresponding capacitor voltages: C_1 (blue) and C_2 (red).

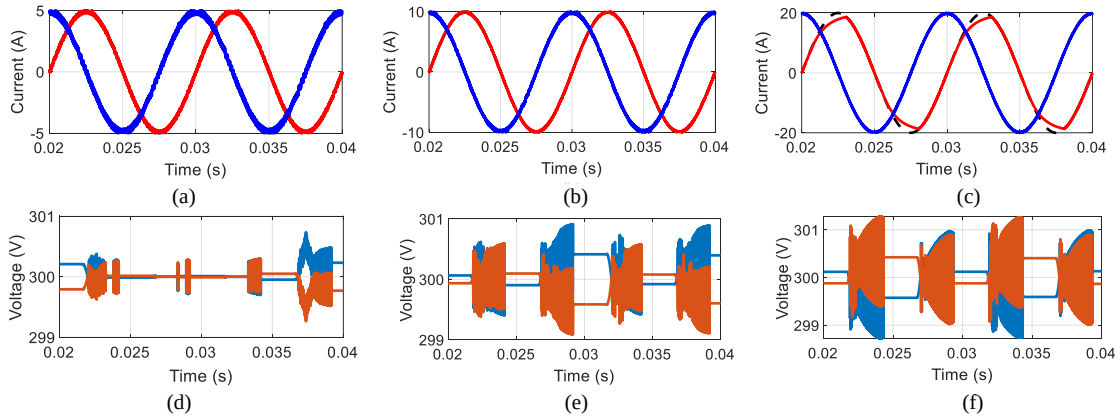

Fig. 11. Simulation results of the PCCT1 scheme: (a)–(c) Currents i_α, i_β for reference amplitudes of 5 A, 10 A, and 20 A; (d)–(f) Corresponding capacitor voltages: C_1 (blue) and C_2 (red).

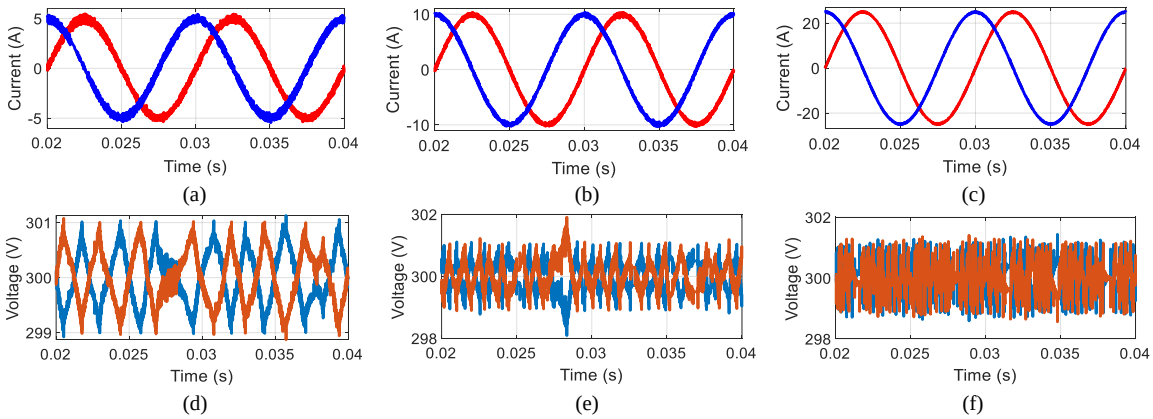

Fig. 12. Simulation results of the PCCT2 scheme: (a)–(c) Currents i_α, i_β for reference amplitudes of 5 A, 10 A, and 20 A; (d)–(f) Corresponding capacitor voltages: C_1 (blue) and C_2 (red).

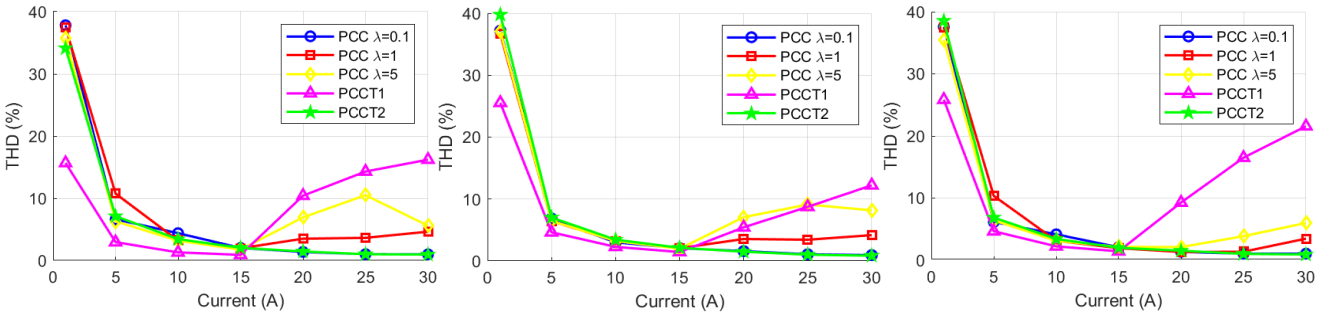

Fig. 13. The THD of the (a) phase-a, (b) phase-b, and (c) phase-c currents is presented for different operating points to compare waveform quality across the control schemes.

The results indicate that in the PCC scheme, reducing λ improves current quality, as reflected by a lower THD. However, this improvement comes at the expense of significantly increased peak-to-peak capacitor voltage, as shown in Fig. 7. The PCCT1 scheme achieves the best current quality among the three; nevertheless, its operating range is limited, and when the load current exceeds approximately 15 A, the tracking capability deteriorates, leading to waveform distortion and a rapid increase in THD. In contrast, the PCCT2 scheme maintains stable current quality with THD comparable to that of PCC at λ = 0.1. This highlights the superior advantages of PCCT2 over conventional PCC, providing equivalent current quality with reduced computational burden and better capacitor voltage balancing, as demonstrated in Fig. 7.

VII. CONCLUSIONS

This paper has successfully developed two control schemes, PCCT1 and PCCT2, which adopt a pre-selection strategy of voltage vectors before being utilised in current prediction calculations. The vector selection tables in each scheme are designed on the basis of different mechanisms: PCCT1 relies on predicted current comparison, whereas PCCT2 emphasises capacitor voltage balancing. As a result, the computational burden is significantly reduced; specifically, PCCT1 requires only four switching states, while PCCT2 employs at most 17 switching states. Furthermore, the need to select weighting factors in the cost function is completely eliminated in both schemes, thereby simplifying the design and implementation of the controllers.

The simulation results demonstrate that both the PCCT1 and PCCT2 schemes achieve stable and robust current tracking, whereas the tracking performance of the PCC scheme varies significantly with the operating point and the weighting factor of the objective function. In terms of load current quality, PCCT1 provides the best performance, but with a limited operating range due to the reduced number of vectors employed. In contrast, PCCT2 achieves a current quality comparable to PCC with a small weighting factor λ, while also ensuring the balancing of the capacitor voltage within the hysteresis band. Conversely, the PCC scheme may lead to considerable capacitor voltage errors.

CONFLICTS OF INTEREST

The authors declare that they have no conflicts of interest.

REFERENCES

[1] M. Gu, Z. Wang, K. Yu, X. Wang, and M. Cheng, “Interleaved model predictive control for three-level neutral-point-clamped dual three-phase PMSM drives with low switching frequencies”, *IEEE Transactions on Power Electronics*, vol. 36, no. 10, pp. 11618–11630, 2021. DOI: 10.1109/TPEL.2021.3068562.

[2] M. Gu, Z. Wang, and O. Dordevic, “Analysis and reduction of current and voltage ripple in DC link for three-level NPC inverter-fed dual three-phase motor drives”, *IEEE Transactions on Power Electronics*, vol. 38, no. 4, pp. 5128–5140, 2023. DOI: 10.1109/TPEL.2022.3224125.

[3] N. S. Nair and M. Barai, “A three-level NPC fed induction motor drive with closed loop dc-link voltage balancing algorithm”, in *Proc. of 2020 International Conference on Power, Instrumentation, Control and Computing (PICC)*, 2020, pp. 1–6. DOI: 10.1109/PICC51425.2020.9362418.

[4] B. Li, H. Tian, L. Ding, X. Wu, G. J. Kish, and Y. R. Li, “An improved three-level neutral point clamped converter system with full-voltage balancing capability for bipolar low-voltage DC grid”, *IEEE Transactions on Power Electronics*, vol. 38, no. 12, pp. 15792–15803, 2023. DOI: 10.1109/TPEL.2023.3318531.

[5] K. Milev, F. Alshammari, V. Yaramasu, M. J. Duran, and K. Yadlapati, “Predictive control with fixed switching frequency for three-level boost and NPC converters interfaced PMSG wind turbine”, in *Proc. of 2020 3rd International Conference on Energy, Power and Environment: Towards Clean Energy Technologies*, 2021, pp. 1–6. DOI: 10.1109/ICEPE50861.2021.9404476.

[6] P. Catalán, Y. Wang, J. Arza, and Z. Chen, “A comprehensive overview of power converter applied in high-power wind turbine: Key challenges and potential solutions”, *IEEE Transactions on Power Electronics*, vol. 38, no. 5, pp. 6169–6195, 2023. DOI: 10.1109/TPEL.2023.3234221.

[7] B. Liu, P. Jain, Q. Zhu, L. Liu, and J. Cao, “Simple algorithm for mitigating neutral point voltage fluctuations (NPVF) in 3L-NPC inverter used for solar applications”, in *Proc. of 2023 IEEE International Conference on Power Electronics, Smart Grid, and Renewable Energy (PESGRE)*, 2023, pp. 1–5. DOI: 10.1109/PESGRE58662.2023.10404724.

[8] J. E. Espinoza, J. R. Espinoza, L. A. Moran, and D. G. Sbarbaro, “A systematic controller design approach for neutral-point-clamped three-level inverters”, in *Proc. of IECON’03. 29th Annual Conference of the IEEE Industrial Electronics Society (IEEE Cat. No.03CH37468)*, 2003, pp. 2191–2196, vol. 3. DOI: 10.1109/IECON.2003.1280583.

[9] L. Liu *et al.*, “A Robust high-quality current control with fast convergence for three-level NPC converters in microenergy systems”, *IEEE Transactions on Industrial Informatics*, vol. 19, no. 11, pp. 10716–10726, 2023. DOI: 10.1109/TII.2023.3241594.

[10] I. M. Alsofyani and K.-B. Lee, “Simple capacitor voltage balancing for three-level NPC inverter using discontinuous PWM method with hysteresis neutral-point error band”, *IEEE Transactions on Power Electronics*, vol. 36, no. 11, pp. 12490–12503, 2021. DOI: 10.1109/TPEL.2021.3074957.

[11] W. Xiong *et al.*, “An algebraic modulation strategy for 3L-NPC converters with inherent neutral-point voltage balance capability”, *IEEE Transactions on Power Electronics*, vol. 37, no. 7, pp. 7533–7539, 2022. DOI: 10.1109/TPEL.2022.3145949.

[12] M. Wu, Y. W. Li, and G. Konstantinou, “A comprehensive review of capacitor voltage balancing strategies for multilevel converters under selective harmonic elimination PWM”, *IEEE Transactions on Power*

Electronics, vol. 36, no. 3, pp. 2748–2767, 2021. DOI: 10.1109/TPEL.2020.3012915.

[13] P. Karamanakos, E. Liegmann, T. Geyer, and R. Kennel, "Model predictive control of power electronic systems: Methods, results, and challenges", *IEEE Open Journal of Industry Applications*, vol. 1, pp. 95–114, 2020. DOI: 10.1109/OJIA.2020.3020184.

[14] M. Khalilzadeh, S. Vaez-Zadeh, J. Rodriguez, and R. Heydari, "Model-free predictive control of motor drives and power converters: A review", *IEEE Access*, vol. 9, pp. 105733–105747, 2021. DOI: 10.1109/ACCESS.2021.3098946.

[15] M. F. Elmorshedy, W. Xu, F. F. M. El-Sousy, Md. R. Islam, and A. A. Ahmed, "Recent achievements in model predictive control techniques for industrial motor: A comprehensive state-of-the-art", *IEEE Access*, vol. 9, pp. 58170–58191, 2021. DOI: 10.1109/ACCESS.2021.3073020.

[16] T. Li, X. Sun, G. Lei, Y. Guo, Z. Yang, and J. Zhu, "Finite-control-set model predictive control of permanent magnet synchronous motor drive systems—An Overview", *IEEE/CAA Journal of Automatica Sinica*, vol. 9, no. 12, pp. 2087–2105, 2022. DOI: 10.1109/JAS.2022.105851.

[17] R. Vargas, P. Cortes, U. Ammann, J. Rodriguez, and J. Pontt, "Predictive control of a three-phase neutral-point-clamped inverter", *IEEE Transactions on Industrial Electronics*, vol. 54, no. 5, pp. 2697–2705, 2007. DOI: 10.1109/TIE.2007.899854.

[18] D. Rojas, M. Rivera, J. Muñoz, C. Baier, and P. Wheeler, "Predictive current control applied to a 3L-NPC inverter", in *Proc. of 2021 IEEE International Conference on Automation/XXIV Congress of the Chilean Association of Automatic Control (ICA-ACCA)*, 2021, pp. 1–7. DOI: 10.1109/ICAACCA51523.2021.9465309.

[19] X. Cai, Z. Zhang, J. Zhang, Z. Li, R. Kennel, and Z. Zhang, "Improved predictive control of three-level-NPC power converters", in *Proc. of 2021 IEEE International Conference on Predictive Control of Electrical Drives and Power Electronics (PRECEDE)*, 2021, pp. 393–402. DOI: 10.1109/PRECEDE51386.2021.9680960.

[20] D. Wang *et al.*, "Model predictive control using artificial neural network for power converters", *IEEE Transactions on Industrial Electronics*, vol. 69, no. 4, pp. 3689–3699, 2022. DOI: 10.1109/TIE.2021.3076721.

[21] S. A. Hossain and Md. Habibullah, "Modulated model predictive current control of three-level NPC inverter with overmodulation capability", in *Proc. of 2020 11th International Conference on Electrical and Computer Engineering (ICECE)*, 2020, pp. 137–140. DOI: 10.1109/ICECE51571.2020.9393100.

[22] W. Song, M. S. R. Saeed, B. Yu, J. Li, and Y. Guo, "Model predictive current control with reduced complexity for five-phase three-level NPC voltage-source inverters", *IEEE Transactions on Transportation Electrification*, vol. 8, no. 2, pp. 1906–1917, 2022. DOI: 10.1109/TTE.2021.3131420.

[23] T. Jin, Y. Huang, Y. Lin, and M.-N. Daniel Legrand, "Model predictive current control based on virtual voltage vector method for parallel three-level inverters", *IEEE Journal of Emerging and Selected Topics in Power Electronics*, vol. 9, no. 5, pp. 6049–6058, 2021. DOI: 10.1109/JESTPE.2021.3061688.

[24] W. Alhosaini, Y. Wu, and Y. Zhao, "An enhanced model predictive control using virtual space vectors for grid-connected three-level neutral-point clamped inverters", *IEEE Transactions on Energy Conversion*, vol. 34, no. 4, pp. 1963–1972, 2019. DOI: 10.1109/TEC.2019.2923370.

[25] A. Ja'afari *et al.*, "Voltage balancing of NPC converter capacitors in FS-MPC method using current sensor with reduction of computational burden", in *Proc. of 2021 IEEE International Conference on Predictive Control of Electrical Drives and Power Electronics (PRECEDE)*, 2021, pp. 218–223. DOI: 10.1109/PRECEDE51386.2021.9680939.

[26] N. H. Viet and P. D. Dai, "Predictive current control with vector selection of a voltage source inverter", in *Proc. of 2023 15th International Conference on Electronics, Computers and Artificial Intelligence (ECAI)*, 2023, pp. 01–06. DOI: 10.1109/ECAI58194.2023.10194158.

[27] H. Dan, Q. Zhu, T. Peng, S. Yao, and P. Wheeler, "Preselection algorithm based on predictive control for direct matrix converter", *IET Electric Power Applications*, vol. 11, no. 5, pp. 768–775, 2017. DOI: 10.1049/iet-epa.2016.0473.

[28] A. Bebboukha *et al.*, "A reduced vector model predictive controller for a three-level neutral point clamped inverter with common-mode voltage suppression", *Scientific Reports*, vol. 14, no. 1, 2024. DOI: 10.1038/s41598-024-66013-0.